Thermomechanical Analysis and Numerical Simulations of Fused Filament Fabricated Polylactic Acid Parts

Irina BUTE *, Sergejs TARASOVS, Jevgenijs SEVCENKO, Andrey ANISKEVICH

The University of Latvia, Institute for Mechanics of Materials, Jelgavas st. 3, Riga, LV-1004, Latvia

http://doi.org/10.5755/j02.ms.35076

Received 12 September 2023; accepted 25 December 2023

This work aimed to investigate the thermal deformation of polylactic acid (PLA) samples 3D-printed by Fused Filament Fabrication. The irreversible thermal strain (ITS) and coefficient of linear thermal expansion (CLTE) of four sets of samples with various sizes and thicknesses of the layer in the three directions of the measurements were investigated. The thermomechanical analysis (TMA) was used for the investigation of thermal deformation. During the study, the dependencies of deformation on temperature were obtained. The samples' CLTE values at various ranges of temperatures were estimated using the obtained dependencies. ITS was observed after heating to 80 °C during the first TMA cycle. The values reached 8 – 9 %. The impact of layer thickness and the number of layers in the sample on ITS was noticed. Shrinkage in the X direction and expansion in the Z direction with almost the same values were observed. Finite element code ANSYS was used to simulate the distribution of temperature and accumulation of residual thermal stresses in the printed part. The correlation was obtained between the level of simulated residual thermal stresses for samples with different number of layers and layer thicknesses and measured ITS after annealing.

Keywords: coefficient of linear thermal expansion, irreversible thermal strain, PLA, FFF, finite element method.

1. INTRODUCTION

The polymers used in Fused Filament Fabrication (FFF) include thermoplastics [1], such as acrylonitrile butadiene styrene (ABS), polylactic acid (PLA), nylon, polycarbonate, high-impact polystyrene, polyethylenimine, chlorinated polyethylene, poly(ether ether ketone), and other. ABS and PLA are the commonly used thermoplastics in the FFF process [2]. PLA material has good mechanical properties (ultimate tensile strength, nominal strain at break, tensile strength), high reliability, and low cost [3, 4]. It is strong but more brittle compared to ABS [5], and it has a lower coefficient of thermal expansion, than ABS.

During the FFF process, the raw material is a filament that is melted, extruded, and applied with a heated nozzle onto the model. After deposition, the material cools, solidifies, and adheres to the surrounding material. The distortion of the part during the print is one of the most important issues in the FFF process. Repeated heating and cooling cycles of additively manufactured parts occur from the layer-by-layer building process. This process leads to residual stress accumulation during part building up, which could affect the shape and dimensions of the 3D-printed product [6]. Some works have shown that 3D-printed parts relieve stress through deformation during printing [7, 8]. The residual stresses of printed parts are removed by annealing. When heated, stress relief leads to deformation of the parts, which remains after cooling and is called irreversible thermal deformation (ITS) [9, 10].

Significant ITS exceeding 20 % was observed in PLA samples after thermal annealing [11]. A simple micromechanical model was proposed in [12, 13] to characterise the dependencies of the ITS on the layer thickness in different directions. The model proposed in these works assumes the tensile force accumulated in each printed strip of the extruded filament in the sample. The value of the force, as well as Poisson's ratio of the material, was fitted to experimental data through standard expressions for the strain of orthotropic materials.

FFF technology involves multi-physical processes, like solidification, heat transfer, and thermo-mechanical deformation. The simulation procedure for FFF technology requires complex coupled analysis with sequential deposition of the material. One of the first finite element models (FEM) for FFF process simulation was developed by Zhang and Chou [14, 15], where the effects of different FFF process parameters on the distortion of printed parts were investigated. The influence of modelling parameters, like time-step and mesh density, and temperature-dependent material properties on the accuracy of the 3D-printed part warpage predictions was studied in [16]. The extensive investigation of the influence of the FFF process and FEM parameters on the predicted temperature distribution and distortion of printed PLA parts was performed in [17].

In our previous work [1], the four thermal characteristics, such as the softening temperature, the coefficient of linear thermal expansion (CLTE), ITS, and the thermal conductivity were estimated and analysed for FFF parts from fourteen different materials at different ranges of temperatures. At estimation of thermal deformation, the ITS of 9 – 10 % of the PLA samples in print X and build Z directions were observed after the heating. The PLA samples had shrinkage along the X-axis and expansion on the Z-axis (Fig. 1). Significant deformation was observed at the range of temperatures 32 – 80 °C.

* Corresponding author. Tel.: +371 24842601.
E-mail: *irina.bute@lu.lv* (I. Bute)

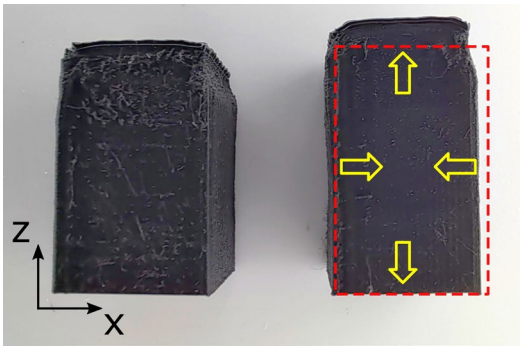

Fig. 1. Example of the sample deformation before (left) and after (right) of the heating, where X and Z axes are print and build direction, respectively

These results prompted detailed research on the thermal behaviour of PLA FFF parts. The aim of the work was to estimate the effect of layer thickness and the number of layers on the irreversible thermal strain and the coefficient of linear thermal expansion of FFF PLA parts at various temperature ranges.

Thermo-elastic finite element analysis was employed in this work to investigate the distribution of the residual thermal stresses in the printed samples and their dependence on the printed layer thickness and the sample's dimensions. Transient thermo-mechanical finite element simulations with progressive element activation were used to simulate the FFF process of the melted material deposition layer by layer on the printing bed, accounting for various process parameters, such as nozzle velocity, extrusion temperature, bed temperature, layer thickness, etc. The results of simulations may form a basis for a qualitative understanding of the internal stresses accumulated in the sample during printing.

2. MATERIALS AND METHODS

2.1. Materials and samples preparation

In this work, the specimens from the filament (PLA Black Devil Design [18]) of 2.85 mm diameter were produced using the Ultimaker S5 printer (Ultimaker B.V., The Netherlands) with a 0.4 mm diameter nozzle. The nozzle and build plate temperatures were 210 °C and 70 °C, respectively. The print head speed was 20 mm/s. The infill pattern was set to "Lines" with infill direction aligned to the X-axis for all layers, and infill density was set to 100 %, fibre width ("Line width") was set to 0.35 mm. These printer settings provided the unidirectional orientation of all filament fibres in all specimens and uniform within any specimen's cross-section. Four sets of samples were prepared to evaluate ITS with layer thicknesses of 0.05, 0.1, 0.2, and 0.3 mm. Each set of samples was printed at sizes of 10 ×10 × 5 mm, 10 × 10 × 10 mm, and 10 × 10 × 15 mm (length × width × height) (Fig. 2).

All samples' sides were lightly polished by using the 320-grit sandpaper at low speed before measuring ITS. The print and build directions are marked as X and Z, respectively (Fig. 3).

2.2. Methods

The CLTE and irreversible thermal strain were determined by thermomechanical analysis (TMA) Expansion mode with a measuring probe (of 3 mm thickness) with ball point performed with Mettler-Toledo TMA/SDTA 841e.

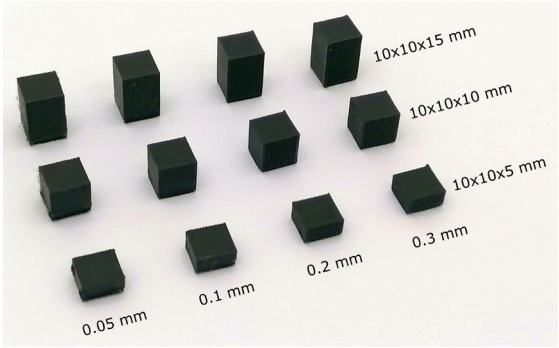

Fig. 2. Illustration of 3D-printed samples

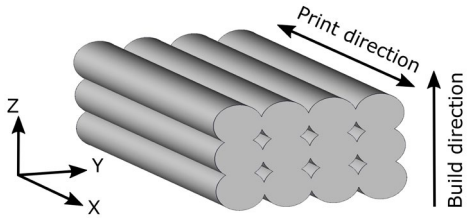

Fig. 3. Illustration of print and build directions of 3D-printed samples

The measurements were carried out in three directions X, Y, and Z. For each direction, a separate test was done, and the different samples were tested because they could not be used after the annealing process. During the investigation, two heating/cooling cycles were completed for the samples at the temperature range from 30 to 140 °C with a heating rate of 1 °C/min according to [19]. Obtained dependencies of displacement on time, and deformation on temperature were used to estimate ITS and CLTE values. An example of the obtained typical dependencies is shown in Fig. 4 and Fig. 5. The ITS values were obtained from the first heating/cooling cycle. The CLTE values were obtained from the second heating/cooling cycle.

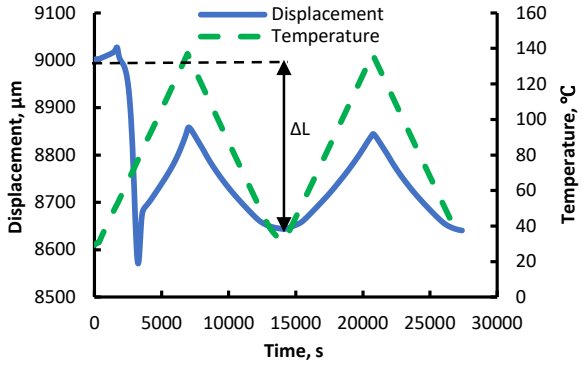

Fig. 4. Typical dependence of displacement and temperature as a function of time during the TMA test in X direction

The ITS was calculated from the displacement values as

$$ITS = \frac{\Delta L}{L_0} \times 100\%, \quad (1)$$

where $\Delta L = L_1 - L_0$ is the change in the dimensions of the specimen; L_0 is the initial length of the specimen (Fig. 4).

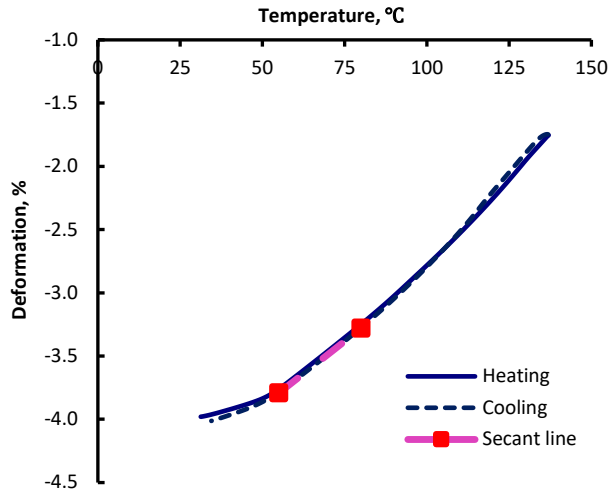

Fig. 5. Typical dependence of deformation on temperature during the second cycle of TMA in X direction (the pink line is the secant line)

The CLTE values α were determined at the various ranges of temperature 32 – 45 °C, 45 – 60 °C, 60 – 75 °C, 75 – 90 °C, 90 – 105 °C, 105 – 120 °C, and 120 – 136 °C. It should be noted that the CLTE is evaluated as described in [19], but in this case, for the simplified evaluation values, uses:

$$\alpha_i = \frac{\Delta L_i}{L_0 \Delta T_i}, \tag{2}$$

where ΔL_i is the change of the specimen length at the range of temperature ΔT_i; L_0 is the initial length of the specimen (Fig. 5).

2.3. Numerical model

General purpose finite element code ANSYS was used to simulate temperature distribution and accumulation of residual thermal stresses in printed part during sequential deposition of melted polymer material on a building plate. Element "birth and death" technique was used to simulate the deposition of new portions of hot material on previously deposited and partially cooled layers. Within this approach, the whole model is divided into finite elements with an initial temperature equal to the temperature of the nozzle. The simulations were conducted iteratively. All elements are killed (deactivated) at the beginning of the analysis. Then they are activated one by one (or several elements simultaneously in one step to minimise computation time) with an initial temperature equal to the specified deposition temperature. Once the element is activated, transient thermal analysis is started for the time interval corresponding to the deposition speed of the material. The resulting temperature distribution is used as a load for mechanical solution and deformation of the deposited elements is calculated. At the next iteration new portion of elements is activated and bonded to previously activated elements with calculated temperature distribution used as the initial condition. At each step, the external boundary of currently active elements is determined, and corresponding initial and boundary conditions are applied:

a) the initial temperature of all inactive nodes is set to the nozzle temperature;

b) bottom nodes of the first layer of elements are fixed to simulate the adhesion of the part to the building plate, and the temperature of these nodes is set to the temperature of the building plate;

c) convection boundary conditions are used for side surfaces of currently active elements.

Fig. 6 shows typical finite element mesh used in simulations and boundary conditions applied at each step during the simulation of the deposition of melted filament. The solution time of each simulation step depended on the printing speed, size of finite elements, and the number of simultaneously activated elements in this step.

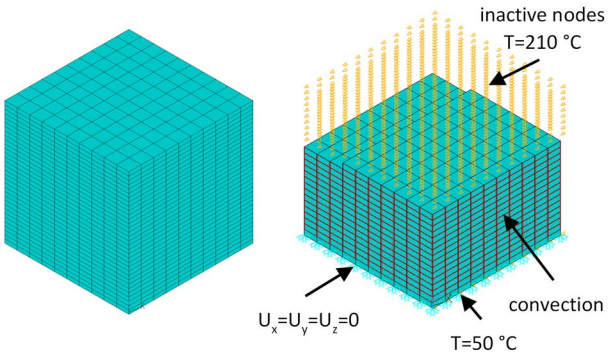

Fig. 6. Finite element model of a cubic sample (left) and boundary condition applied at each solution step (right).

After the printing, the part was allowed to cool down to room temperature with fixed displacements at the bottom surface. In the last step of the analysis, the part was unglued from the printing plate by releasing the displacement constraints at the bottom nodes (three corner nodes remain fixed in a certain direction to suppress rigid body movement).

Deformations and residual stresses of the numerical model at the end of the simulation represent the internal state of the printed part and allow us to predict warpage and even potential failure of the part during printing due to accumulated thermal stresses.

As shown in [16], the temperature-dependent elastic material properties of PLA polymer should be used to simulate the 3D printing process. Elastic modulus at different temperatures was measured using the DMA technique (Mettler-Toledo TMA/SDTA 861e, tensile mode 5 N, frequency of 1Hz from 30 to 140 °C at a heating rate of 3K per min) for the 3D-printed samples with the sizes 19.5 × 4 × 1.1 mm, and a layer thickness of 0.35 mm. The typical results for a storage modulus, loss modulus, and loss factor are shown in Fig. 7. Two relaxation temperatures (near 60 and 110 °C) seen on the tan δ curve are due to glass transition and cold crystallisation. The CLTE at elevated temperatures was also measured in this work and will be presented in the next section. Thermal conductivity and heat capacity of PLA samples at room temperature were measured in a previous study [1], and constant values were used in this work in numerical simulations.

The air temperature inside the printing chamber during printing was measured by a thermocouple at different positions, and an average temperature of 35 °C was obtained. The temperature of the sample during printing was

monitored by an infrared camera (RS PRO RS-9875, RS Components, Corby, United Kingdom).

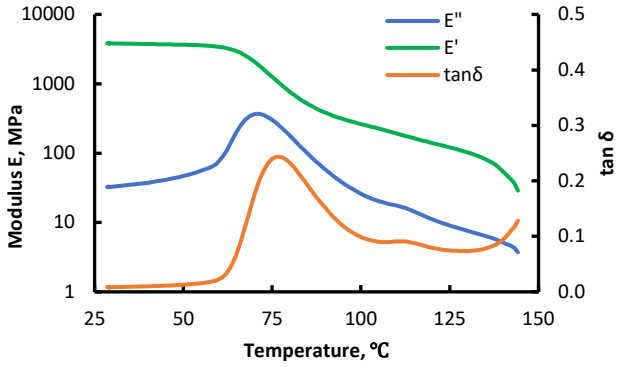

Fig. 7. Typical DMA curve of the PLA samples (E' is storage modulus, E'' is loss modulus and tan δ is loss factor)

A comparison of experimentally measured temperature with numerical simulations is presented in Fig. 8, where the temperature distribution at the end of the printing process for a sample with dimensions 10 × 10 × 10 mm, a layer thickness of 0.3 mm, and a printing speed of 10 mm/s is shown. The heat transfer coefficient of forced convection in the printing chamber was determined by fitting the results of simulations to the observed temperature distribution on the external surface of the sample during printing. A transient thermal solution with the element "birth" technique and boundary conditions described above was used for simulations. The best results were obtained for the forced convection heat transfer coefficient equal to 700 W/(m^2 K).

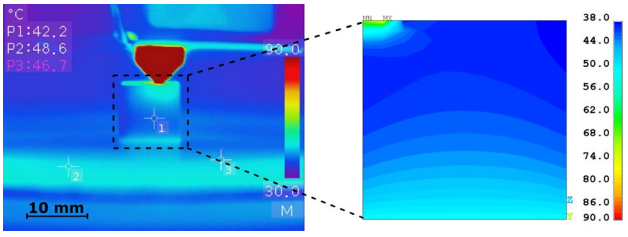

Fig. 8. Measured (left) and simulated (right) temperature distribution (°C) on the surface of the sample during printing

The heat transfer coefficient of free convection for 3D-printed samples (for cooling of the samples after printing) was determined by a separate set of numerical simulations and fitting results to experimental data of Joule heating of samples with embedded conductive track [20], and the best fit was obtained for a heat transfer coefficient equal to 15 W/(m^2 K).

3D thermal solid 8-node elements (SOLID70) were used in the transient thermal solution for fitting the temperature distribution, and coupled-field SOLID5 elements were used for the transient thermal-elastic solution. Elements with dimensions 1 × 1 mm in XY plane and thickness corresponding to the actual layer thickness for each sample were used for simulations so that one row of 10 elements roughly corresponds to three rows of deposited filament (infill line distance of 0.35 mm was used for printing). The elements were activated by blocks of 10 elements for each solution step to minimise solution time.

3. RESULTS AND DISCUSSION

3.1. Coefficient of linear thermal expansion

The CLTE of the test samples in three directions, X, Y, and Z, were determined. A significant deformation was observed during the first cycle, as shown in Fig. 4. Therefore, the CLTE values were determined in the second cycle.

The dependence of CLTE values in three directions on different temperature ranges is demonstrated in Fig. 9. As can be seen from the diagram, the significant diference of the CLTE values between X and Y, Z - directions was observed. For example, CLTE in the X direction is about 1.3 – 1.4 times larger than in the Y and Z directions at temperatures above 90 °C.

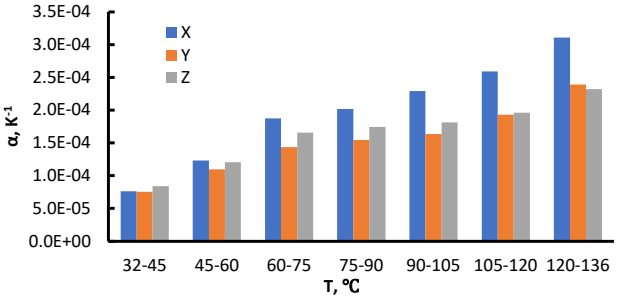

Fig. 9. Values of CLTE at different temperature ranges (size of cubes 10 × 10 × 10 mm and layer thickness of 0.2 mm)

This phenomenon can probably be explained by the effect of cold crystallisation of the material and the orientation of macromolecules within the layer. Cold crystallisation is associated with the expansion of macromolecules due to increased mobility during heating [21]. Polymer molecules tend to orient parallel to the extrusion direction within the layer [22], which in our case, corresponds to the X direction.

The CLTE of printed samples at various layer thicknesses and temperature ranges in the X direction was presented in Fig. 10. CLTE values rapidly increased at 32 – 60 °C (1.6 – 1.8 times) and 1.2 – 1.5 at 105 – 136 °C. The difference between CLTE values (1.2 – 1.3 times) at the thicknesses of layer 0.05 and 0.2 mm at 45 – 60 °C and 105 – 120 °C ranges of temperatures was found. These significant differences in values in certain temperature ranges indicate transition regions, like glass transition and crystallisation (*Tg* and *Tc*).

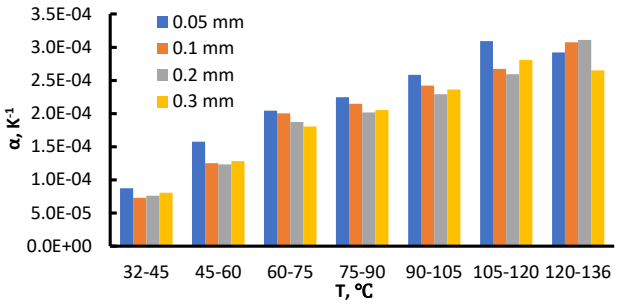

Fig. 10. Values of the CLTE at X direction at different temperature ranges and layer thicknesses (size of samples 10 × 10 × 10 mm)

This assumption is confirmed by the DSC study of PLA samples in [1]. At the transition temperatures, the material's structure changes, affecting the values of CLTE.

As was expected, there was no dependence of CLTE on the number of layers, as shown by the estimation of this relation (Fig. 11).

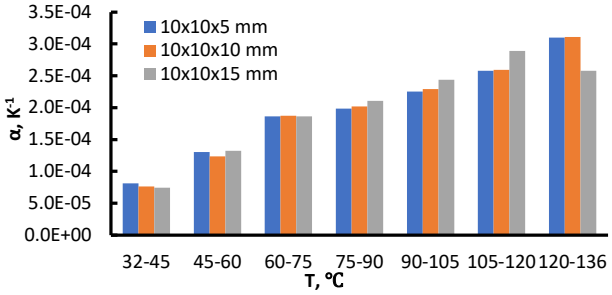

Fig. 11. Values of CLTE at X direction at different temperature ranges and sample heights (layers thickness 0.2 mm)

The difference between the values of CLTE at heating and cooling cycles could be near 20 %. Values of the CLTE at the heating were lower than at the cooling **(**Fig. 12.**)**. During the cooling, the time to rebuild the structure is longer than during the heating Fig. 4.

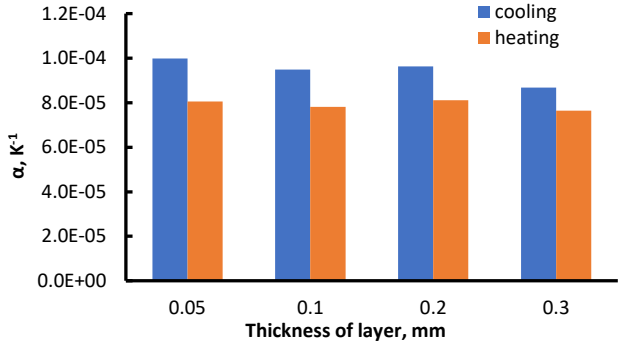

Fig. 12. Values of CLTE at heating and cooling cycles, with different layer thicknesses (size of samples 10 × 10 × 10 mm, X – direction).

3.2 Thermal deformation

During the study, the thermal deformation of FFF samples was investigated. In Fig. 13, the dependence of the deformation on temperature in the first heating/cooling cycle of TMA is shown.

The figure shows that the whole process can be divided into 4 stages. The first stage is uniform expansion – range of temperature 30 – 50 °C; the second stage is the rapid change of deformation of the sample, 50 – 60 °C. The third stage is the intensive change of the deformation 75 – 80 °C. The shrinkage on the X-direction and the expansion on the Z-direction (approx. 8 %) were observed during the second and third stages. The last stage above 80 °C is the monotonous expansion in all directions. The relaxation process started at 50 and ended at 80 °C, corresponding to the temporary shape temperature and recovery temperature of PLA polymer [23], respectively. The curves on the diagram Fig. 13 have two bends at approx. 57 °C and 80 °C. The first bend could be characterised by the glass transition temperature, where PLA is in a glassy state, and its chain mobility is very small. That's why the deformation in this range of temperature is small. The second is the ending of the relaxation process temperature (*Trel*). During the heating above *Tg*, intermolecular connections are destroyed; hence the mobility of the links and flexibility of the chains are increased. During this process, the deformation rapidly increases (Fig. 13). Cold crystallisation visible on DMA curves near 110 °C in Fig. 7 was not observed in the deformation curve because it has a negligible effect on the thermal expansion, probably due to the low degree of crystallinity measured by the DSC method on similar samples in the previous study [1].

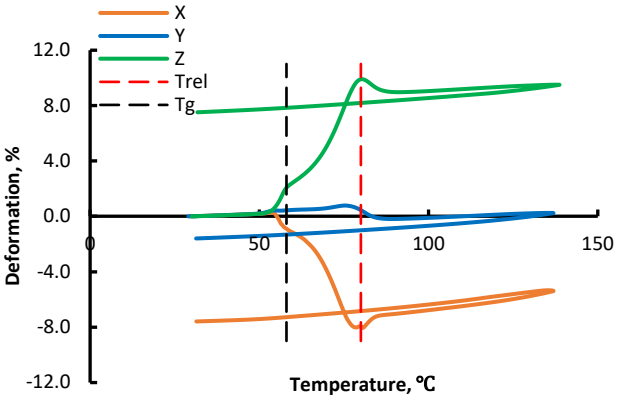

Fig. 13. Dependence of the deformation on temperature for the sample in X, Y, and Z directions. The layer thickness was 0.05 mm, and the sample size was 10 × 10 × 15 mm

The irreversible thermal strain of the 3D-printed samples with three kinds of sizes (10 × 10 × 5, 10 × 10 × 10, and 10 × 10 × 15 mm) with various layer thicknesses (0.05, 0.1, 0.2, and 0.3 mm) in 3 directions of measurement (X, Y, and Z) was investigated.

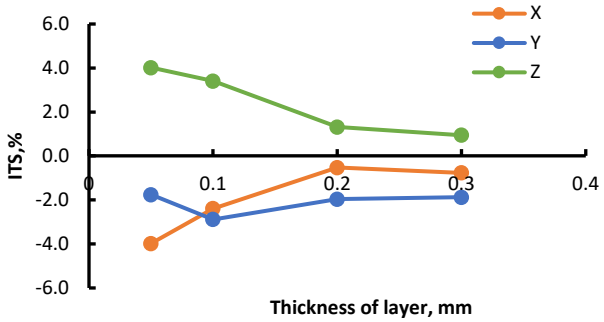

Fig. 14. ITS for several layer thicknesses for X, Y, and Z directions. Sample size 10 × 10 × 10 mm

As can be seen from Fig. 14, the ITS depends on the layer thickness in the X and Z directions, except in the Y direction. Values of ITS are very close at layer thicknesses of 0.2 and 0.3 mm. Shrinkage in the X direction and expansion in the Z direction with almost the same values was observed. Shrinkage in the X-axis could be the result of the relief of the residual stress. Most of the printed tracks laid down were printed parallel to the X-axis. The residual thermal stress and strain occur along the road direction because shrinkage is more along than perpendicular to the print direction. The almost the same but opposite values of the ITS in the Z-direction can be explained by Poisson's effect. During the study, the dependences of ITS of samples on height (5, 10, and 15 mm) at the various thicknesses of the layer and for three directions were obtained (Fig. 15).

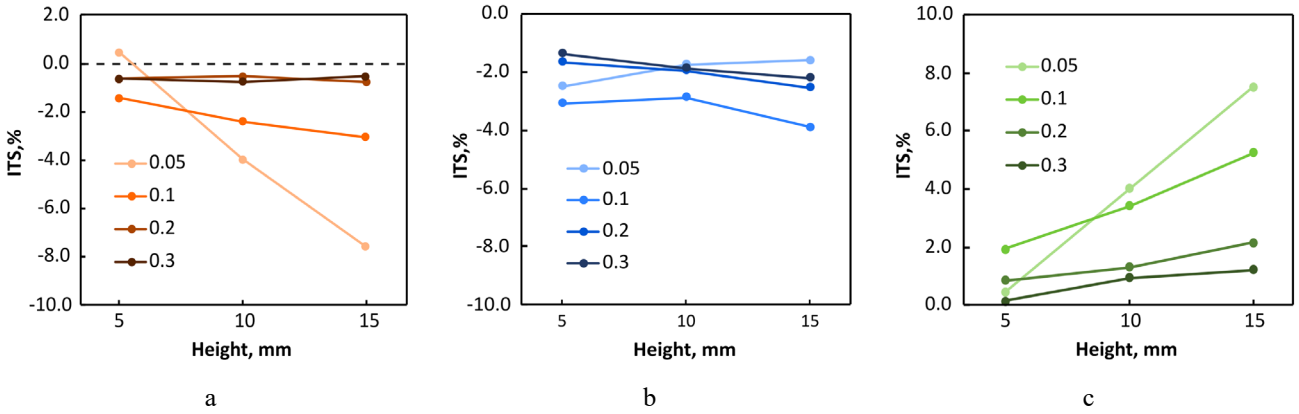

Fig. 15. Dependence of ITS on the height of samples with several layer thicknesses (0.05, 0.1, 0.2, and 0.3 mm): a – X direction of measurement; b – Y direction of measurements; c – Z direction of measurements

The impact of layer thickness and the number of layers in the sample on ITS exists. The biggest deformation (nearly 8 % in directions X and Z in the case of the sample's height of 15 mm) was observed at a layer thickness of 0.05 mm.

The correlation between ITS, layer thickness and number of layers was indicated in [7, 11]. D'Amico and others note that thermal deformation is the result of thermal stress relief, which builds on the surfaces between layers. The smaller the layer thickness, the more layers fit per unit length. Therefore, as the layer thickness decreases, the build-up of intra-layer and inter-layer thermal stress increases.

3.3. Numerical simulations

Transient thermo-elastic simulations were used to model residual stress distribution within the printed part. Models with different dimensions and layer thicknesses were analysed to investigate the influence of geometrical parameters on residual stress levels.

Fig. 16 shows the distribution of residual thermal stresses in the cubic samples with a height of 10 mm and different layer thicknesses. As shown results of simulations, the compressive zone is developed in the middle of the cooled samples, which is compensated by tensile stresses in a relatively thin zone at the surfaces of the cube. A similar picture is observed in all directions, with stresses in the Z direction being significantly higher than in other directions. This fact may explain the expansion of the samples in the Z direction after thermal annealing observed experimentally. Also, it could be noted that residual stresses become larger for thinner layers and a similar trend was observed experimentally in ITS for samples with different thicknesses of printed layers (Fig. 14).

It could be noted that tensile residual stresses developed at the surfaces of the samples have different distributions for stresses acting in X/Y and Z directions. For stresses in X and Y directions tensile zone develops at the top and bottom surface of the cube and has quite uniform distribution. Whereas for stresses in Z direction tensile zones are mainly located near the side edges of the cube and are significantly larger in value. This explains a common defect of 3D-printed parts: layer delamination and splitting during or shortly after the printing [24].

The residual stresses in the X and Y directions obtained in current simulations are quite similar, contrary to experimental data, where ITS in the X and Y directions were significantly different. The current numerical model cannot prognosis different behaviour of samples in the XY plane.

To investigate the dependence of the ITS on specimen dimensions, e.g. height, simulations with a constant layer thickness (0.2 mm) and height of the samples equal to 5, 10, and 15 mm were performed. The results are presented in Fig. 17 for samples with heights equal to 5 and 15 mm (results for 10 mm cube were shown in Fig. 16 in the middle row). Results of simulations show that higher residual stresses are accumulated in larger samples; therefore, higher deformations could be expected during annealing, as was observed in experiments.

The absolute values of numerically obtained residual stresses are quite large, a few times larger than the tensile strength of the PLA samples [25]. As was shown in [16], plasticity with temperature-dependent yield stress should be used in simulations to obtain realistic stresses in the FFF process. Such data is not easy to measure experimentally; therefore, elastic material behaviour used in the current study can be used only for qualitative analysis. It should be noted, however, that even such large residual stresses could not explain ITS of the order of 10 %. As was shown in [1] for samples manufactured from many different materials, typical values of ITS were below 1.5 %, which could be attributed to residual thermal stresses, except samples made from CPE and some brands of PLA polymers, where ITS up to 10 % were measured. Different physical mechanisms are probably responsible for the large ITS of the PLA samples. Shear-induced alignment of polymer chains [26] or shape memory properties of PLA polymer, extensively studied for PLA FFF structures [27], could be responsible for significant irreversible strain during thermal annealing. However, most published works investigate the programming and shape-recovery of post-printed structures [28 – 30] to study the shape-recovery efficiency for various stimuli. Modelling of shape memory effects (strain storage) during the printing process is still in the early stage of development [31].

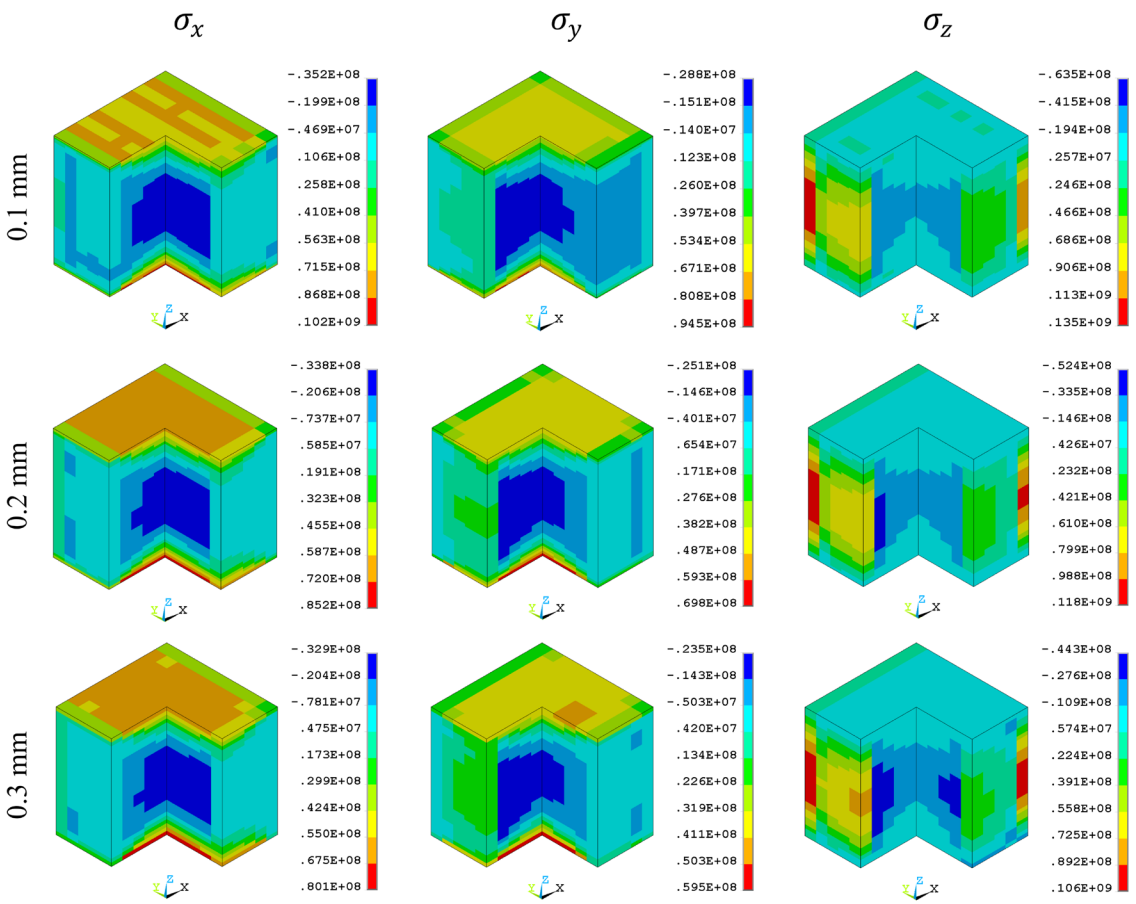

Fig. 16. Simulated residual thermal stresses (Pa) inside 10 × 10 × 10 mm PLA samples with layer thicknesses of 0.1, 0.2, and 0.3 mm

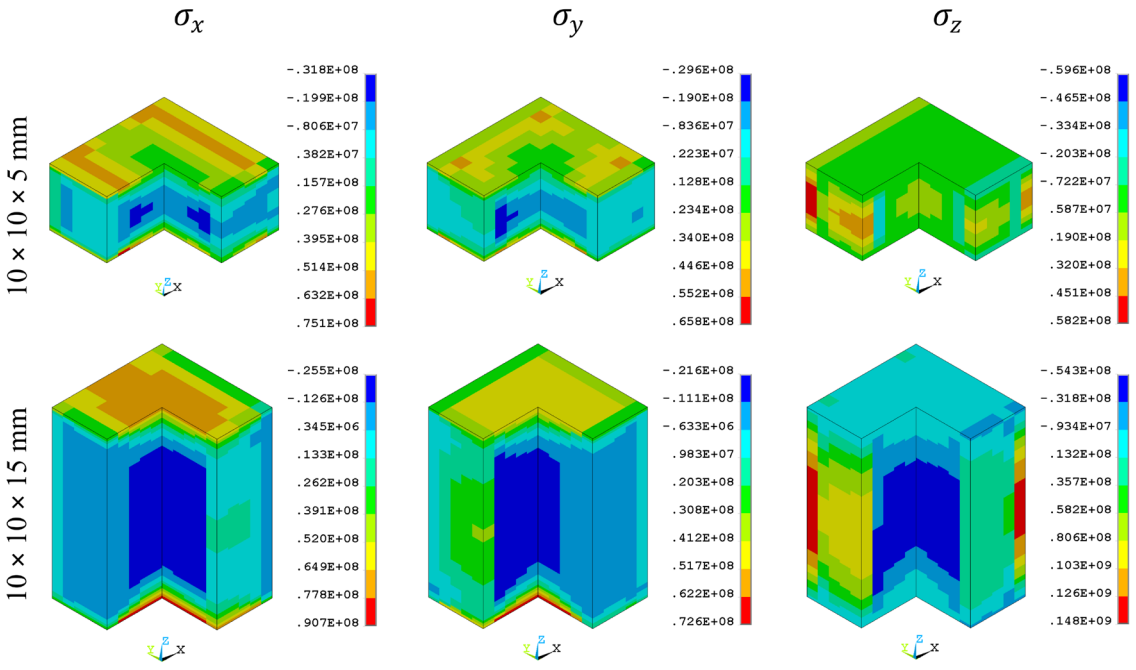

Fig. 17. Simulated residual thermal stresses (Pa) inside PLA samples for different heights (layer thickness of 0.2 mm)

4. CONCLUSIONS

During the research work, the effect of layer thickness, and the number of layers on CLTE and ITS at the various ranges of temperature was investigated.

CLTE values were measured at different temperatures and a rapid increase of CLTE was observed at temperature ranges of 32 – 60 °C and 105 – 136 °C. The values of CLTE at heating were 20 % lower than at the cooling cycles. The analysis of CLTE values at various temperature ranges showed a significant difference in the CLTE measured in Y/Z and X directions. The CLTE in print direction (X) is about 1.3 – 1.4 times larger than in the Y and Z directions at a temperature higher than 90 °C.

Significant irreversible thermal strain was observed in the samples after the first TMA cycle. Accumulation of ITS started at temperatures close to the glass transition temperature of PLA material (approx. 60 °C) and reached its maximum at 80 °C, followed by reversible thermal expansion at subsequent heating. Observed ITS values in the X and Z directions were significantly higher than in the Y direction, reaching 8 % strain and showing shrinkage along the print direction and expansion in the build direction. The highest ITS was observed for samples with the smallest layer thickness and larger dimensions in the Z direction.

Numerical modelling of the printing process using temperature-dependent elastic properties of PLA polymer showed that accumulated residual thermal stresses inside the printed sample strongly depend on the layer thickness and the total number of layers. Results of simulations show the correlation between residual thermal stresses accumulated during printing and subsequent cooling of the sample and experimentally measured irreversible thermal strain released during thermal annealing. However, high ITS values observed for PLA samples in the current study cannot be explained solely by the relaxation of residual thermal stresses during annealing. Shear-induced alignment of the polymer chains during material deposition and solidification with relaxation upon thermal annealing above T_g or shape memory effects need to be included in the numerical model for the correct representation of observed ITS.

Acknowledgements

This research was supported by ERDF Project No. 1.1.1.1/19/A/031 "OPTITOOL, Decision Tool for Optimal Design of Smart Polymer Nanocomposite Structures Produced by 3D Printing".

REFERENCES

1. **Bute, I., Tarasovs, S., Vidinejevs, S., Vevere, L., Sevcenko, J., Aniskevich, A.** Thermal Properties of 3D Printed Products from the Most Common Polymers *The International Journal of Advanced Manufacturing Technology* 124 (7) 2023: pp. 2739 – 2753. https://doi.org/10.1007/s00170-022-10657-7
2. **Ngo, T.D., Kashani, A., Imbalzano, G., Nguyen, K.T.Q., Hui, D.** Additive Manufacturing (3D Printing): A Review of Materials, Methods, Applications and Challenges *Composites Part B: Engineering* 143 2018: pp. 172 – 196. https://doi.org/10.1016/j.compositesb.2018.02.012
3. **Lanzotti, A., Grasso, M., Staiano, G., Martorelli, M.** The Impact of Process Parameters on Mechanical Properties of Parts Fabricated in PLA with an Open-Source 3-D Printer *Rapid Prototyping Journal* 21 (5) 2015: pp. 604 – 617. https://doi.org/10.1108/RPJ-09-2014-0135
4. **Wittbrodt, B., Pearce, J.M.** The Effects of PLA Color on Material Properties of 3-D Printed Components *Additive Manufacturing* 8 2015: pp. 110 – 116. https://doi.org/10.1016/j.addma.2015.09.006
5. **Hafsa, M.N., Ibrahim, M., Wahab, M.S., Zahid, M.S.** Evaluation of FDM Pattern with ABS and PLA Material *Applied Mechanics and Materials* 465 – 466 2014: pp. 55 – 59. https://doi.org/10.4028/www.scientific.net/AMM.465-466.55
6. **Nyiranzeyimana, G., Mutua, J.M., Mose, B.R., Mbuya, T.O.** Optimization of Process Parameters in Fused Deposition Modelling of Thermoplastics: A Review *Materialwissenschaft und Werkstofftechnik* 52 (6) 2021: pp. 682 – 694. https://doi.org/10.1002/mawe.202000193
7. **Wang, T.M., Xi, J.T., Jin, Y.** A Model Research for Prototype Warp Deformation in the FDM Process *The International Journal of Advanced Manufacturing Technology* 33 (11) 2007: pp. 1087 – 1096. https://doi.org/10.1007/s00170-006-0556-9
8. **Casavola, C., Cazzato, A., Moramarco, V., Pappalettera, G.** Residual Stress Measurement in Fused Deposition Modelling Parts *Polymer Testing* 58 2017: pp. 249 – 255. https://doi.org/10.1016/j.polymertesting.2017.01.003
9. **Kantaros, A., Karalekas, D.** Fiber Bragg Grating Based Investigation of Residual Strains in ABS Parts Fabricated by Fused Deposition Modeling Process *Materials & Design* 50 2013: pp. 44 – 50. https://doi.org/10.1016/j.matdes.2013.02.067
10. **Riggins, A.W., Dadmun, M.D.** Controlling Residual Stress in Material Extrusion 3D Printing through Material Formulation *Additive Manufacturing* 73 2023: p. 103678. https://doi.org/10.1016/j.addma.2023.103678
11. **D'Amico, A., Debaie, A., Peterson, A.** Effect of Layer Thickness on Irreversible Thermal Expansion and Interlayer Strength in Fused Deposition Modeling *Rapid Prototyping Journal* 23 (5) 2017: pp. 943 – 953. https://doi.org/10.1108/RPJ-05-2016-0077
12. **D'Amico, T., Barrett, C., Presing, J., Peterson, A.M.** Micromechanical Modeling of Irreversible Thermal Strain *Additive Manufacturing* 27 2019: pp. 91 – 98. https://doi.org/10.1016/j.addma.2019.02.019
13. **D'Amico, T., Barrett, C., Presing, J., Patnayakuni, R., Pourali, M., Peterson, A.** Harnessing Irreversible Thermal Strain for Shape Memory in Polymer Additive Manufacturing *Journal of Applied Polymer Science* 136 (47) 2019: pp. 48239. https://doi.org/10.1002/app.48239
14. **Zhang, Y., Chou, Y.K.** Three-Dimensional Finite Element Analysis Simulations of the Fused Deposition Modelling Process *Proceedings of the Institution of Mechanical Engineers, Part B: Journal of Engineering Manufacture* 220 (10) 2006: pp. 1663 – 1671. https://doi.org/10.1243/09544054JEM572
15. **Zhang, Y., Chou, K.** A Parametric Study of Part Distortions in Fused Deposition Modelling Using Three-Dimensional Finite Element Analysis *Proceedings of the Institution of Mechanical Engineers, Part B: Journal of Engineering Manufacture* 222 (8) 2008: pp. 959 – 968. https://doi.org/10.1243/09544054jem990

16. **Cattenone, A., Morganti, S., Alaimo, G., Auricchio, F.** Finite Element Analysis of Additive Manufacturing Based on Fused Deposition Modeling: Distortions Prediction and Comparison with Experimental Data *Journal of Manufacturing Science and Engineering* 141 (1) 2018: pp. 011010. https://doi.org/10.1115/1.4041626
17. **Trofimov, A., Le Pavic, J., Pautard, S., Therriault, D., Lévesque, M.** Experimentally Validated Modeling of the Temperature Distribution and the Distortion During the Fused Filament Fabrication Process *Additive Manufacturing* 54 2022: pp. 102693. https://doi.org/10.1016/j.addma.2022.102693
18. Devil Design PLA Filament: Data Sheet https://devildesign.com/download/PLA_-_product_card.pdf Access date: 14.11.2023
19. **ASTM E831-12** Standard Test Method for Linear Thermal Expansion of Solid Materials by Thermomechanical Analysis. 2012.
20. **Stankevich, S., Sevcenko, J., Bulderberga, O., Dutovs, A., Erts, D., Piskunovs, M., Ivanovs, V., Ivanov, V., Aniskevich, A.** Electrical Resistivity of 3D-Printed Polymer Elements *Polymers* 15 (14) 2023: pp. 2988. https://doi.org/10.3390/polym15142988
21. **Senatov, F.S., Niaza, K.V., Zadorozhnyy, M.Y., Maksimkin, A.V., Kaloshkin, S.D., Estrin, Y.Z.** Mechanical Properties and Shape Memory Effect of 3D-Printed PLA-Based Porous Scaffolds *Journal of the Mechanical Behavior of Biomedical Materials* 57 2016: pp. 139 – 148. https://doi.org/10.1016/j.jmbbm.2015.11.036
22. **Es-Said, O.S., Foyos, J., Noorani, R., Mendelson, M., Marloth, R., Pregger, B.A.** Effect of Layer Orientation on Mechanical Properties of Rapid Prototyped Samples *Materials and Manufacturing Processes* 15 (1) 2000: pp. 107 – 122. https://doi.org/10.1080/10426910008912976
23. **Cerbe, F., Sinapius, M., Böl, M.** Methodology for FDM 4D Printing with Thermo-Responsive Smps *Materials Today: Proceedings* 2022, In Press. https://doi.org/10.1016/j.matpr.2022.11.440
24. **Sbriglia, L.R., Baker, A.M., Thompson, J.M., Morgan, R.V., Wachtor, A.J., Bernardin, J.D.** Embedding Sensors in FDM Plastic Parts During Additive Manufacturing. In: Topics in Modal Analysis & Testing, Volume 10, Mains, M. Ed., Springer International Publishing, Cham, 2016: pp. 205 – 214.
25. **Zīle, E., Zeleniakiene, D., Aniskevich, A.** Characterization of Polylactic Acid Parts Produced Using the Fused Deposition Modelling *Mechanics of Composite Materials* 58 (2) 2022: pp. 169 – 180. https://doi.org/10.1007/s11029-022-10021-6
26. **Costanzo, A., Spotorno, R., Candal, M.V., Fernández, M.M., Müller, A.J., Graham, R.S., Cavallo, D., McIlroy, C.** Residual Alignment and Its Effect on Weld Strength in Material-Extrusion 3D-Printing of Polylactic Acid *Additive Manufacturing* 36 2020: pp. 101415. https://doi.org/10.1016/j.addma.2020.101415
27. **Zhang, J., Yin, Z., Ren, L., Liu, Q., Ren, L., Yang, X., Zhou, X.** Advances in 4D Printed Shape Memory Polymers: From 3D Printing, Smart Excitation, and Response to Applications *Advanced Materials Technologies* 7 (9) 2022: pp. 2101568. https://doi.org/10.1002/admt.202101568
28. **Ma, S., Jiang, Z., Wang, M., Zhang, L., Liang, Y., Zhang, Z., Ren, L., Ren, L.** 4D Printing of PLA/Pcl Shape Memory Composites with Controllable Sequential Deformation *Bio-Design and Manufacturing* 4 (4) 2021: pp. 867 – 878. https://doi.org/10.1007/s42242-021-00151-6
29. **Liu, H., He, H., Huang, B.** Favorable Thermoresponsive Shape Memory Effects of 3D Printed Poly(Lactic Acid)/Poly(E-Caprolactone) Blends Fabricated by Fused Deposition Modeling *Macromolecular Materials and Engineering* 305 (11) 2020: pp. 2000295. https://doi.org/10.1002/mame.202000295
30. **Mehrpouya, M., Vahabi, H., Janbaz, S., Darafsheh, A., Mazur, T.R., Ramakrishna, S.** 4D Printing of Shape Memory Polylactic Acid (PLA) *Polymer* 230 2021: pp. 124080. https://doi.org/10.1016/j.polymer.2021.124080
31. **Akbar, I., El Hadrouz, M., El Mansori, M., Lagoudas, D.** Continuum and Subcontinuum Simulation of FDM Process for 4D Printed Shape Memory Polymers *Journal of Manufacturing Processes* 76 2022: pp. 335 – 348. https://doi.org/10.1016/j.jmapro.2022.02.028